Soft Matter

Cite this: *Soft Matter*, 2011, **7**, 6444

www.rsc.org/softmatter

PAPER

Depletion interactions caused by polydisperse, hard platelets

Christoph July,[a] Dzina Kleshchanok[b] and Peter R. Lang*[a]

Received 11th March 2011, Accepted 21st April 2011
DOI: 10.1039/c1sm05429e

We investigate depletion interactions near a wall caused by polydisperse silica-coated gibbsite platelets, using total internal reflection fluorescence microscopy (TIRF) to characterize the sphere–wall interaction potential. As no theoretical model for polydisperse platelets exists, we extend a model for monodisperse depletant cylinders by assuming negligible thickness and averaging over the disc size distribution, finding nearly perfect matching with experimental data. The resulting averaged depletion potentials have, as predicted by the extended model, the same depth as monodisperse potentials, but differ in range and shape according to the size distribution. We compare mean particle sizes and standard deviations derived by TIRF with results from TEM measurements.

1 Introduction

Depletion interactions arise when colloids of different size or shape are mixed in a suspension.[1] The depth of the depletion interaction potential depends on the concentration (number density) of the depletant, which is generally the smaller particle species, while its range depends on the depletant size. Thus, the shape of an interaction potential can be effectively tuned by choosing various shapes, sizes and concentrations of depletant agents.

Depletion forces are of particular interest in biological systems and have a wide range of technical applications due to their high degree of tunability.[2] They are used to govern self-organization or induce phase transitions, *e.g.* crystallization of proteins[3,4] and aggregation of colloids.[5] Prominent examples of depletants are spheres or rods,[6,7] since they are theoretically well described.[8,9] For technical/industrial applications though, a common choice as a depletant is a polymer such as dextran[10] or polyethylene oxide,[11] since they are much easier to synthesize in comparison. However, polymers are rather ineffective depletant agents as compared to anisotropic colloids such as rod- or plate-like particles. This is due to the fact that the depth of the potentials is dictated by the number density and shape of the depleting particle species. For example in the extreme case of depletion caused by very thin long rods, aside from the number density, only the length governs the strength of the depletion forces. Long rods therefore show very strong depletion effects at low mass concentrations as compared to polymers or other spherical objects of the same size dimension and mass concentration. While depletion interaction potentials of colloidal rods had been measured directly before,[12–16] rigid colloidal platelets have, to our knowledge, not yet been investigated in a direct depletion study, although platelets are widely present in nature (clay minerals, red blood cells, *etc.*) and can be synthesized in a controlled manner in the laboratory (mixed metal hydroxides, gibbsite, *etc.*). The most prominent examples of colloidal platelets are natural clays,[17] which are widely used as rheological modifiers for surface coatings, paints, and drilling fluids.[18–20] Their rheological applications are based on the microscopic structural properties, originating from the highly anisotropic shape of the colloids and the inter-particle interactions. However, due to the flexibility and the large polydispersity in both size and shape, clay particles are hard to describe theoretically.[17]

In the present work we therefore chose a synthetic platelet type, which was developed in the van't Hoff laboratory in Utrecht. The colloidal particles are composed of gibbsite (γ-$Al(OH)_3$) and resemble platelets with a hexagonal shape and a thickness significantly smaller than the diameter of the circle enclosing them. Their synthesis is described in detail elsewhere.[21]

Being of inorganic origin facilitates sample handling of the platelets, in contrast to biological samples such as fd-virus,[22,23] a common choice of a model system for monodisperse, thin rods, since the particles require almost no special solvent conditions and offer stability in a broad spectrum of solvents.[24]

To probe the depletion interaction induced by gibbsite platelets, total internal reflection fluorescence microscopy (TIRF)[25,26] is used, which is very closely related to total internal reflection microscopy (TIRM).[27,28] A brief overview over TIRF will be given later. TIRM is an established method for accurately measuring depletion potentials between a probe sphere and a flat wall. Earlier TIRM measurements of depletion forces induced by boehmite rods,[15] fd-virus,[12,23] polymeric depletants, *e.g.* polyethylene oxide[11,29] and spherical depletant agents, such as PNIPAM particles,[30,31] show that TIRM is the method of choice when measuring weak interaction potentials. TIRF is equally

[a]*Forschungszentrum Jülich GmbH, ICS–3, 52425 Jülich, Germany. E-mail: p.lang@fz-juelich.de; Fax: +49 (0)2461 61 2280; Tel: +49 (0)2461 61 4248*
[b]*Van't Hoff Laboratory for Physical and Colloid Chemistry - Debye Research Institute, Utrecht University, Utrecht, Netherlands*

well suited for this task as will be discussed in the experimental section. Moreover, it removes scattered light originating from the depletant and background by imperfect interfaces. In the course of the presented work, it will be shown that gibbsite platelets cause slight turbidity in the sample, giving TIRF a small advantage over TIRM.

This is, to our knowledge, the first experimental study to show depletion attractions characteristic of colloidal platelets interacting only by excluded volume. The first direct measurement on platelet-depletion[32] was done by Odiachi *et al.* using laponite clays. Their work states that the depletion is completely dominated by the electrical double layer of the highly charged laponite clays and the disc-like shape has no discernible effect on the depletion potentials. Recent works also show that laponite tends to be patchy, aggregates, and forms layer structures, thereby not exhibiting a disk-like shape.[33,34] In this work we show that gibbsite depletants can be successfully described by a theoretical model of infinitely thin, hard platelets.[35] However, the moderate polydispersity of gibbsite platelets sets some challenge comparing measurements and theory, since the aforementioned model only makes predictions for monodisperse systems. We overcome this obstacle by extending the theoretical description for the monodisperse case to polydisperse systems by averaging with respect to a size distribution of platelet diameters.

2 Experimental

2.1 Setup, measurement principle and data evaluation

The TIRF setup consists of a home-built TIR microscope, assembled from standard microscopy components (Olympus), which are mounted on a X-95 rail system (Linos). The basic principle along with steps of the data analysis, is sketched in Fig. 1. An infinity corrected 40× Olympus SLCPlanFl objective with a focal length of $f = 6.5$–8.3 mm and a numerical aperture NA = 0.55 is used.

The fluorescence light from the probe sphere inside the sample cell is separated from the illumination light by an edge pass filter ($\lambda_{pass} > 515$ nm) (chroma E515LPv2) and projected onto a CCD-camera (Photometrics Cascade 1 K). Using fluorescence and the filter increases the signal-to-noise-ratio well beyond $S/N > 4000$.

The sample cell is a quartz glass flow cell (QS137) from Hellma with a volume of 26 µl and a thickness of 100 µm. For exchanging liquids during a measurement series the cell is connected to a glass syringe with a valve by highly chemically resistive tubing (Tygon 2075 from Saint Gobain).

The illumination source is a 10 mW Diode–Laser ($\lambda_{ex} = 440$ nm) mounted on a goniometer, driven by a stepper motor, which allows the angle of incidence α_i to be set with a high degree of accuracy and reproducibility. A prism, made of BK7 glass from Edmond optics is attached to the cell to enable total reflection conditions and the creation of an evanescent wave. Possible gaps between prism and cell are bridged with a thin film of immersion oil so that the refractive index is matched. An angle $\alpha_i = 63.41°$ is chosen for the experiments, which yields a penetration depth, $\beta^{-1} = 150$ nm, of the evanescent field intensity.

In the course of an experiment, fluorescing spherical probe particles ($R = 2.5$ µm thermo scientifc G0500) are injected into the measurement cell. These float at an average elevation in the range of 100 nm above the reflecting interface, and are illuminated by the evanescent field. Multiple particles may be observed at the same time with a CCD-camera, provided that the distance between them is large enough to prevent mutual influence.

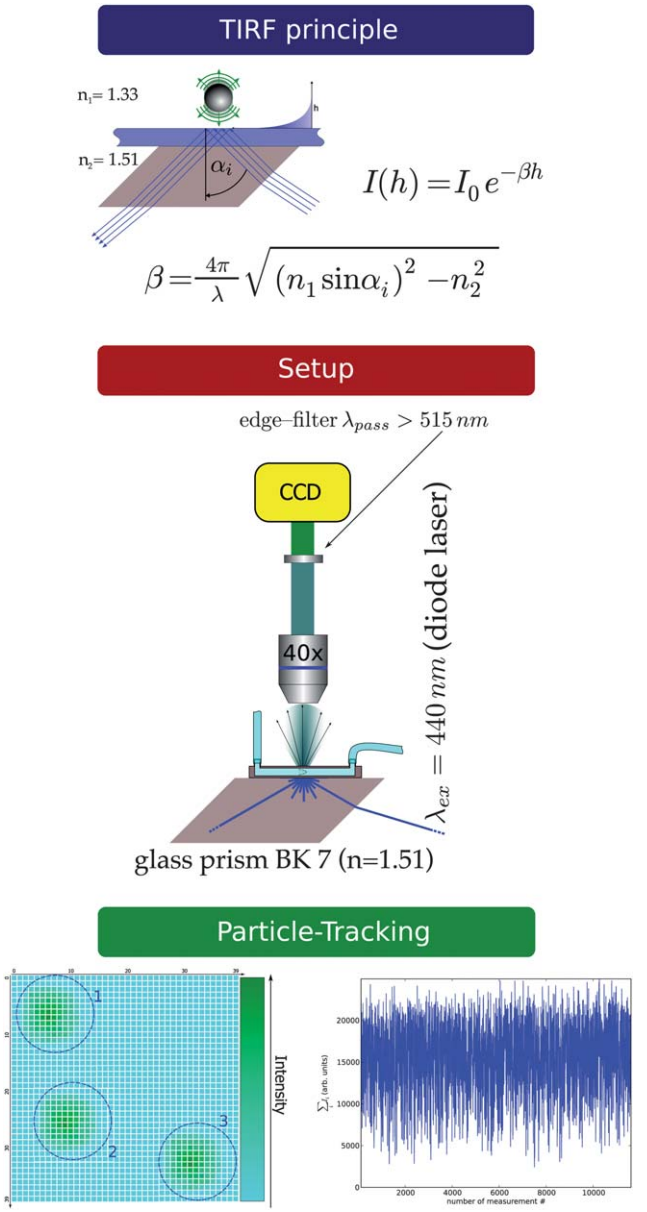

Fig. 1 Principle: Basic idea of an evanescent illumination along with the equations relating intensity to height; Setup: schematic of the setup, listing the components employed; Particle Tracking: cartoon visualizing how the picture data is converted to intensity values by use of a particle tracking algorithm.

Under the assumption that the fluorophore inside the spheres is never completely saturated, which is well warranted by the comparison in Fig. 2, each individual particle's change in elevation directly converts into a change in fluorescence intensity due to the evanescent nature of the illumination as suggested by eqn (1). For the given experimental parameters, *i.e.* low penetration depth and p-polarization of the incident beam, the illumination profile can be sufficiently well described by an exponential:[36,37]

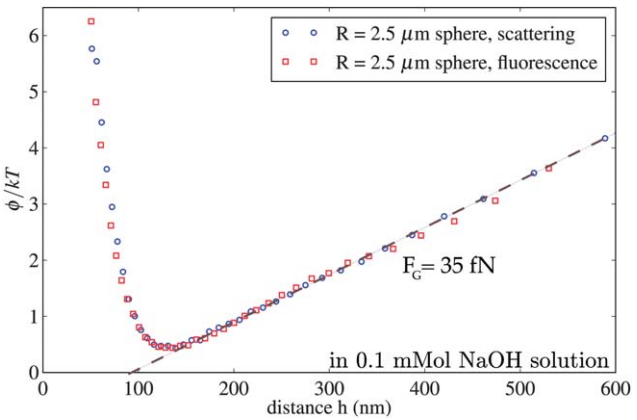

Fig. 2 Comparison of sphere–wall interaction potentials (without depletant) for a $R = 2.5\mu m$ sphere measured fluorescently and by scattering. In the case of the scattering-based measurement, the fluorescence light was blocked by a filter. The measurement principle is described in Fig. 1 and the corresponding section. There is virtually no difference between the two measurements, and no indication of bleaching, since that would create an artifact, manifesting itself as a deformation of the potential.

$$I(h) = I_0 \exp(-\beta h) \tag{1}$$

with

$$\beta = \frac{4\pi}{\lambda_{ex}}\sqrt{(n_1 \sin\alpha_i)^2 - n_2^2}. \tag{2}$$

Here, the refractive index $n_1 = 1.51$ is that of the glass cell, while n_2 is the refractive index of the liquid, usually 1.33 for aqueous solutions. The intensity I_0 signifies the fluorescence intensity at zero elevation and is usually determined by adding enough salt (NaCl) to the solution to screen all electrical interactions and thereby allowing the particles to sediment. The knowledge of I_0 is required to enable normalization of elevations to absolute scale.

To analyse the data gathered by TIRF, it is necessary to define an effective intensity trace. For this purpose, all particles, i, in the field of view are tracked with a particle tracking algorithm developed by John Crocker and David Grier.[38] The code not only yields the position on the CCD-chip, but also the intensity at any given time. To compute an effective intensity trace the recorded particle traces are put through an exclusion filter to remove false hits by checking the mean value and the variance of each individual intensity trace. We define a selection window for the filter based on the most likely average mean intensity of an individual trace observed during an experiment, allowing a variation of 5 percent. Once that is done all selected intensity traces are summed up, $I_{tot} = \sum_i I_i$, to make up an effective single particle intensity trace.

Treating all particles as effectively one particle, makes it possible to utilize the fact that the particles perform their motion according to Boltzmann statistics. The probability density, $p(h)$, of finding a particle at an elevation h can be written as,

$$p(h) = B\exp\left(\frac{-\phi_{tot}(h)}{k_B T}\right) \tag{3}$$

where ϕ_{tot} is the total sphere–wall interaction potential. Following the analysis of Prieve,[28] it is assumed that the probability of observing a given intensity is equal to the probability of finding a particle at the corresponding elevation, *i.e.* $p(h)dh = p(I)dI$. Together with eqn (1) this leads to,

$$p(h) = -\beta p(I) I(h). \tag{4}$$

The probability density $p(I)$ is determined experimentally, assuming that the histogram of measured intensities $N(I)$, converges to $p(I)$ for small enough bins and a sufficiently large number of events. Dividing the resulting probability density of heights $p(h)$ by $p(h_0)$ we obtain,

$$\Delta\phi(h) = \ln\left(\frac{N_{max} I_{max}}{N(I) I}\right). \tag{5}$$

Here N_{max} is the number of counts in the histogram maximum, I_{max} is the corresponding intensity, $\Delta\phi(h) = \phi(h) - \phi(h_0)$ and $\phi(h_0)$ is an arbitrarily defined value of the potential minimum which is located at h_0. Up to this point no specification of the sphere–wall potential's functional form has been made. The only constraint of the method is that the measured probe particles have to be in thermodynamic equilibrium.

Without a depletant the bare sphere–wall interaction potential is correctly described by the superposition of an electrostatic repulsion in the Debye–Hückel–Derjaguin approximation and a gravitational force $F_G = m \cdot g$, as $\phi_{ref}(h) = A\exp(-\kappa h) + F_G h$. Here A is the amplitude of the electrostatic repulsion, κ^{-1} is the Debye screening length, m is the buoyancy corrected particle mass and g is the acceleration due to gravity. Adding platelets results in an additive depletion potential and the total potential is expressed as $\phi_{tot}(h) = \phi_{ref}(h) + \phi_{dep}(h)$, where

$$-\frac{\phi_{dep}(h)}{kT} = \begin{cases} \frac{2}{3}\pi\rho_N R D^2 f(h,D) & \text{for } h \le D \\ 0 & \text{for } h > D \end{cases}. \tag{6}$$

with

$$\rho_N = \frac{c_{plate} N_A}{M_{plate}}$$

$$f(h,D) = \left[\frac{3}{2}\frac{h}{D}\arcsin\frac{h}{D} - \frac{3}{4}\pi\frac{h}{D} + \left(1 + \frac{1}{2}\left(\frac{h}{D}\right)^2\right)\sqrt{1 - \left(\frac{h}{D}\right)^2}\right].$$

In this expression for the depletion potential[35,39] caused by platelets, the platelets are regarded as infinitely thin discs with diameter D. The platelet concentration is given by c_{plate} in units of mass per volume, N_A is Avogadro's number, M_{plate} the platelets' molar mass, and R is the radius of the probe sphere. Strictly, this formula is only valid for monodisperse platelet solutions. In our experiments this is not the case. That means the given equation has to be modified to account for a distribution $S(D)$ of platelet sizes. We neglect any variation in the thickness of the real platelets, since it does not contribute significantly to the theoretical potential. To get an expression for polydisperse platelets, we average the potential in eqn (6) with respect to a size distribution, where it is assumed that the platelet size follows a log normal distribution,

$$S(D,\bar{D},\sigma_D)=\frac{1}{\sqrt{2\pi}\sigma D}\exp\left(-\frac{(\ln D-\mu)^2}{2\sigma^2}\right) \quad (7)$$

$$\sigma=\sqrt{\ln\frac{\sigma_D^2}{\bar{D}^2}+1} \quad (8)$$

$$\mu=\ln\bar{D}-\frac{\sigma^2}{2} \quad (9)$$

where $\bar{D}$ is the expectation value of the disc diameter and σ_D is the corresponding standard deviation. To get a mean depletion potential this distribution is convoluted with the potential for a monodisperse system:

$$\overline{\phi}_{dep}(h)=\int_0^\infty S(D,\bar{D},\sigma_D)\phi_{dep}(h,D)dD \quad (10)$$

To average the potential, the total particle number density ρ_N is required. However, it is not directly accessible because we only have the concentration c_{plate} of a polydisperse system, which only gives the mass of all particles in solution independent of their size.

In order to calculate the total particle number density we exploit the fact that, the size distribution is connected to the mass distribution.[40] The mass of one particle is given by $m_i=\pi(D/2)^2L\rho_{gibb}$ where L is the thickness of a platelet. The total mass concentration is described by

$$c_{plate}=\sum_{i=1}^{N}c_i=\frac{1}{V}\sum_{i=1}^{N}m_i=\frac{N\pi L\rho_{gibb}}{4V}\sum_{i=1}^{N}D_i^2 \quad (11)$$

Knowing that $D_i=D_i-\bar{D}+\bar{D}$ and the definition of σ_D^2 this reduces to

$$c_{plate}=\frac{N\pi L\rho_{gibb}}{4V}(\bar{D}^2+\sigma_D^2) \quad (12)$$

which yields:

$$\rho_N=\frac{4c_{plate}}{\pi L\rho_{gibb}(\bar{D}^2+\sigma_D^2)}. \quad (13)$$

Now that all contributions are known the integral expression makes it possible to fit data measured from a polydisperse system. By use of a Levenberg–Marquardt fitting algorithm, $\bar{D}$ and σ_D can be derived for a given concentration c_{plate} and a material density ρ_{gibb}.

In order to measure a pure depletion potential, a reference potential of bare spheres without any depletant present has to be measured first. The data of the bare spheres are fitted with the superposition of electrostatic interaction and a gravitational potential. Subtracting this potential from measurements with platelets present will give the pure depletion potentials $\phi_{dep}(h)=\phi_{tot}(h)-\phi_{ref}(h)$.

For the sake of clarity it is imperative to note that there is no way to measure absolute potentials. The energy values are always relative, without a given point of reference. For example, we could declare the potential to be zero at elevation zero. Yet this wouldn't be very instructive to visualize depletion potentials. Instead, to achieve better comparability, we ignore the zero value of the potential altogether and take the gravitational branch as a reference. Due to the finite range of the depletion interaction it is obvious that the potentials have to overlap for distances larger than some effective disc diameter. In this region, where the potential values coincide and ϕ_{dep} is zero, it is expected that the potentials exhibit the same shape, namely the same linear slope stemming solely from the gravitational force. Consequently the magnitude of all potentials is chosen such that they will have the same value in this region. In the presented figures the raw data are shifted accordingly along the energy axis to fulfill this requirement.

2.2 Sample preparation

Gibbsite platelets with diameter $\bar{D}=212\pm56$ nm and thickness $L=6\pm10$ nm, as determined by TEM, were synthesized according to the standard procedure described elsewhere.[21,41] The platelets were coated with silica[41] to give them a negative surface charge and thereby avoid adhesion to the glass cells. The mass concentration is determined by drying a small amount of suspension and weighing the remaining solid. For the TIRF measurement the solution is diluted with purified water ($\rho_R=18$ MΩcm, total organic contents less than 2 ppb) to the desired concentration, while the ionic strength is set by adding NaOH (Sigma Aldrich 0.1 mol) during dilution, so that the final platelet suspension contains 1 mmol l^{-1} NaOH. Also, fluorescent polystyrene micro spheres ($R=2.5$ μm thermo scientific G0500) are mixed with the sample while diluting to supply probes for the measurement.

The glass cells are thoroughly cleaned by immersion in a mixture of 1 : 1 H_2O_2 (30 vol%) and H_2SO_4 (99 vol%) for over one hour. Afterwards the cells are rinsed with pure water ($\rho_R=18$ MΩcm) and blown dry with dried N_2. This procedure delivers very clean surfaces of the sample cells, free of any residual contamination. Syringes and tubes are cleaned by sonicating them successively in acetone, ethanol and pure water for approximately half an hour, each step.

2.3 TEM measurements

TEM measurements are carried out with a Phillips CM200 at an acceleration voltage of 160–200 kV. The samples are prepared by dip-coating carbon coated copper TEM grids in a highly diluted platelet suspension. The grids are dried at room temperature.

2.4 TIRF measurements

The first step in the experiment is to inject spheres with only solvent (water with 1 mmol l^{-1} NaOH) into the measurement cell. This is done with a syringe connected to the cell by a valve and tubing. Once the spheres are inside and all drift movement inside the cell ceases after closing the valve, a measurement is performed. Usually it is sufficient to use an illumination time of 10 ms per frame with the gain of the EM–CCD turned on. 50000 pictures are recorded with around 5 particles present in the field of view. Due to their relatively large size the lateral movement of the particles during the acquisition period is minimal. Normally a measurement takes of the order of one hour, since the readout time is around 50 ms per frame with these settings. Once a measurement is completed, the solvent is exchanged and a solution with a given platelet concentration is inserted. This procedure is repeated for all platelet concentrations. After the

measurement series has been completed the fluorescence intensity originating from a sticking sphere I_0 is recorded. For this purpose the cell has to be thoroughly rinsed with pure water to remove the platelets before trying to stick a sphere. If this is not done the platelets will cover the glass interface and introduce an error when taking the contact intensity. Having rinsed the cell with pure water, a 0.1 mol l^{-1} NaCl solution with suspended spheres is pumped into the cell. Under these conditions the electrostatic interactions are completely screened and the particles will sediment, sticking irreversibly to the glass surface. Image data of the sticking spheres and the rest of the measurement data are then processed *via* particle tracking to gather intensity traces, which are converted into potentials as described.

The refractive index of gibbsite, $n = 1.58$,[42] deviates sufficiently from water to create turbid aqueous suspensions at rather low concentrations. Using thin measurement cells helps to alleviate that problem. Nevertheless, the turbidity of a sample with finite gibbsite platelet concentrations is large enough that a detectable amount of fluorescence light is absorbed/scattered by the suspension before leaving the sample cell, effectively decreasing the observed intensity. Therefore data recorded in the presence of platelets cannot be referenced to the intensity, I_0, of a sticking sphere, leading to a systematic error in distance. The obvious solution is to index-match the solvent and platelets. However, with the current setup we are limited to a maximum refractive index of the solvent of $n = 1.45$, while gibbsite has a refractive index of $n = 1.58$. Instead of modifying the setup and changing the sample environment, the problem is circumvented by exploiting the fact that the depletion potential is limited to a finite separation distance h_r. Knowing the distance of the reference potential minimum and the size of the platelets leaves only a single choice for the real distance-dependence of a potential, when fitting the model.

To prove equal suitability of the TIRM- and TIRF-methods, in Fig. 2, a potential taken with each of the methods, consisting of electrostatic repulsion and gravity, is shown. They both give the same potential. Further, the slope of the linear branches indicates a weight force of 35 fN for the particle, which agrees with the buoyancy corrected mass of a polystyrene sphere with a radius of $R = 2.5$ μm.

TIRF offers a better signal-to-noise-ratio than TIRM, and the fluorescence intensity is less dependent on the particle size than the scattering intensity. Since a camera is used, better statistics may be achieved in a shorter amount of time, because it is possible to observe multiple particles at the same time.

While having overall favorable properties there are some drawbacks to using TIRF. Depending on the dye, there can be the possibility of bleaching when working with too high illumination intensities. The shown comparison displays no such effect with the employed probing particles.

3 Results and discussion

3.1 TEM measurements of platelets

TEM measurements of platelets are performed as an additional check, whether the platelets are free of aggregates and to acquire knowledge of the size distribution. Some well defined polystyrene spheres with a diameter of 100 ± 4.5 nm are added to the particle suspension to achieve higher accuracy of the analysis (Fig. 3).

Collecting particle sizes from a number of images yields the distribution which is shown in Fig. 4, together with two continuous distribution curves. The latter have been calculated, assuming a logarithmic–normal distribution (eqn (9)) using the values for $\bar{D}$ and σ_D as determined from TEM image analysis and TIRF measurements (see Table 1), respectively.

The calculated distribution functions describe the experimental histogram, with regard to the large statistical errors of the experimental data, equally well. Further, we may conclude that a log–norm distribution is appropriate to describe the size polydispersity of the gibbsite platelets.

Some particles are overlapping, but in none of the pictures can real aggregates be found. So it can safely be assumed that depletion in the TIRF experiments is only caused by singular objects and not by aggregates. For the analysis of the TIRF data, the irregular hexagonal particles are approximated as circular cylinders with the tips of the hexagon touching the bordering circle. This leads to a discrepancy in shape between model and real particles and results in a 17 percent volume difference when assuming regular hexagons.

3.2 TIRF measurements

Interaction potentials with and without depletion induced by silica coated gibbsite platelets between a green fluorescing probe sphere ($R = 2.5$ μm) and a wall are shown in Fig. 5. The figure shows that the depletion parts of the potentials are very pronounced for higher platelet concentrations. As previously discussed, the gravitational branch of all potentials has to be the same for distances higher than the range of the depletion interaction, namely for elevations greater than the disc diameter. Because only relative potentials are measured, the raw data have to be shifted in energy to be physically reasonable. The potentials in Fig. 5 are shifted by −0.65 kT, −1.3 kT and −3 kT with respect

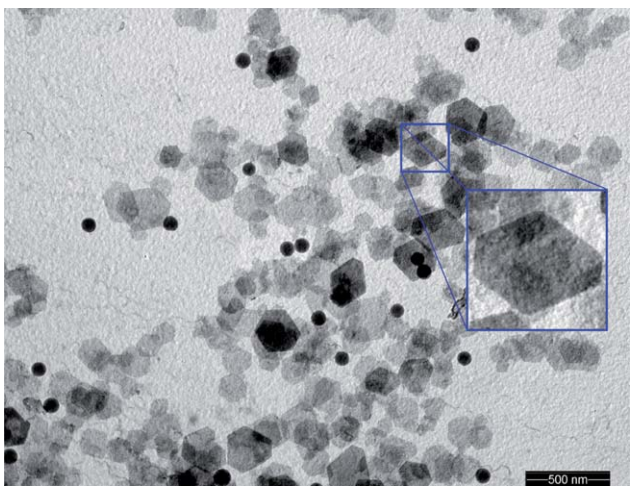

Fig. 3 TEM picture of platelets dried on a carbon coated copper TEM-grid together with polystyrene norm-spheres with $R = 50$ nm. One of the platelets is magnified. The platelets have an irregular hexagonal shape. Multiple pictures are taken to determine the size distribution of the platelets.

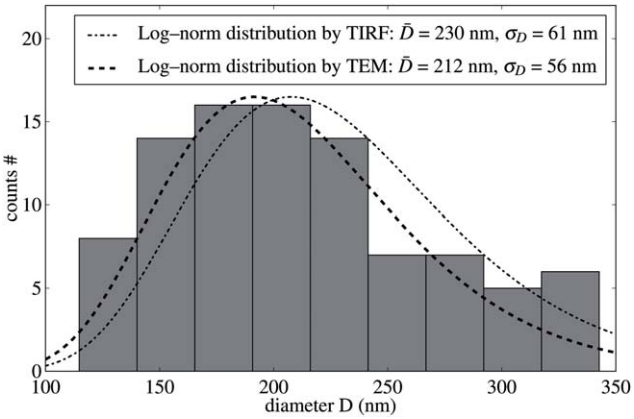

Fig. 4 Size distribution, found by TEM measurements, represented by the histogram and the dashed curve. The shape of the distribution justifies the assumption of a log–normal distribution. For comparison the size distribution found by TIRF is plotted as the point–dashed curve.

Table 1 Summary of fit parameters, comparing fitted concentrations to those determined by weighing

c_{set} (mg ml^{-1})	c_{fit} (mg ml^{-1})	$\bar{D}$ (nm)	σ_D (nm)
3.60	3.94	216	27
6.00	6.60	230	61
12	13.8	247	34

to the reference potential and increasing concentration. The total potentials are displayed with corresponding fits, given as dashed lines. The data are well described by the provided model.

The model prefactor, $c_{fit}/L\rho_{gibb}$, is overestimated roughly by ten percent compared to the values which are calculated from L = 6 nm, ρ_{gibb} = 2.4 g cm^{-3} [42] and the mass concentration c_{set} determined by drying and weighing the stock solution (see Table 1). This is very likely due to the discrepancy in the particles' volume. According to the discussion in Section 3.1 the volume is 17% larger than when only regular hexagons are considered and the idealization of disc like particle shape is used. Furthermore, the thickness, L, of the cylindrical platelets has an uncertainty which cannot be quantified, while the mass density was confirmed by independent measurements.

Pure depletion potentials, obtained by subtraction of the parameterized reference potential from the experimental curves measured at finite platelet concentrations, are shown in Fig. 6. The overall potential shape agrees with the theoretical prediction and the data are described very well by the fit of the theoretical model. The shape does not deviate significantly from the monodisperse case. Concentrations used to fit the data have to be set about ten percent higher than those determined by weighing due to the shape mismatch to achieve a satisfying result.

A remarkable point is that the contact value doesn't change with polydispersity or disc diameter for a system of platelets, which is different from the findings with rods as depletant. This is explained by the applied model. For a monodisperse system the contact value is given by

$$\phi^0_{dep} = \frac{2}{3}\pi\rho_N RD^2 = \frac{8}{3}\frac{cR}{L\rho_{gibb}} \qquad (14)$$

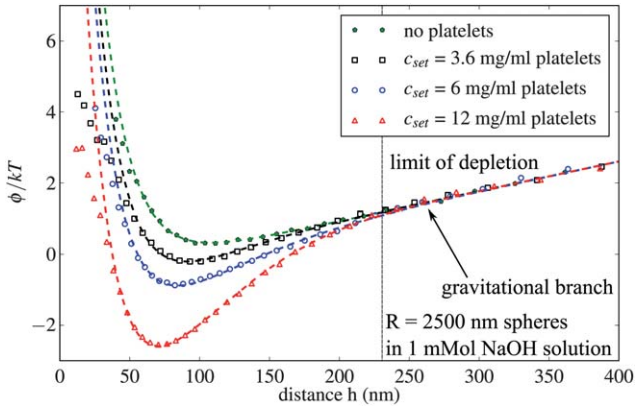

Fig. 5 Full sphere–wall interaction potentials for different platelet concentrations with corresponding fits, given as dashed lines. Potentials with depletion are shifted to match with the gravitational branch of the reference potential: for distances higher than the range of the depletion potential (limit annotated), the potentials have to overlap with respect to their gravitational branches.

and even for polydisperse systems the contact value is independent of the particle diameter. This can easily be shown in an analytical way for an arbitrary distribution function ψ. By definition:

$$\tilde{\sigma}^2 = \int_0^\infty (x-\tilde{\mu})^2\psi(x)dx$$
$$= \int_0^\infty (x^2 - 2\tilde{\mu}x + \tilde{\mu}^2)\psi(x)dx \Rightarrow \int_0^\infty x^2\psi(x)dx = \tilde{\mu}^2 + \tilde{\sigma}^2$$

here $\tilde{\sigma}$ is some standard deviation and $\tilde{\mu}$ is the mean value of the distribution. With this general relation it follows by eqn (6) and (13) that

$$\bar{\phi}^0_{dep} = \int_0^\infty S(D,\bar{D},\sigma_D)\phi^0_{dep}(D)dD$$
$$= \frac{8}{3}c_{plate}R/(L\rho_{gibb}). \qquad (15)$$

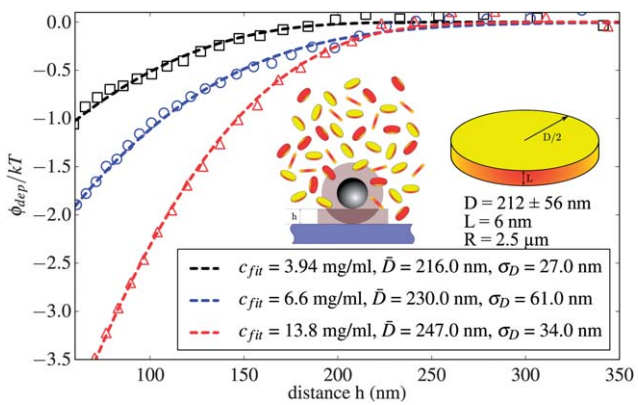

Fig. 6 Pure depletion potentials with corresponding fits for spheres (R_S = 2.5 μm) in platelet solution with different concentrations. The concentrations given here are the ones used to yield a satisfying fit. 1 mmol l^{-1} NaOH has been added to the solution to set the screening length.

Except for the polydispersity in thickness there is no effect on the contact value. The thickness variation can mostly be neglected since the effect on the mass is less pronounced. The derivation shows that the contact value is also independent of type and shape of the size–distribution.

When comparing the distribution functions derived from the TIRF measurements to those obtained by TEM image analysis, some potential error sources have to be considered. However, they are difficult to quantify in detail. Slight sedimentation of the platelets inside the measurement cell over the course of an experiment increases the local concentration. The effect of this issue is rather small, which is seen when a set of spheres is observed over a long period of time. Having imperfect probe–spheres introduces yet another uncertainty into the data. Further error sources are: not strictly homogeneous illumination of the measurement cell and change of the Debye screening length over time due to CO_2 adsorption into the solvent. In addition statistics tend to be poor for $h < 30$ nm and $h > 350$ nm. The potentials in Fig. 6 are cut off at these separations to account for these limitations.

The major error sources are given by low statistics of the TEM measurement and irregularity of shape. The results of the TIRM and the TIRF measurements agree well, within the boundaries of their individual errors, which are estimated to be well larger than 15 percent. The mean diameter measured with TEM is overall smaller, probably an artifact of bad statistics. Another explanation for the generally larger diameter of the discs when determined by TIRF might be that the charge of the platelets was not taken into account. There are existing theoretical predictions for depletion of oblate spheroids, including the electrical double layer.[43] In our case the double layer is of the order of the screening length (about 10 nm). Yet considering an error of over 15 percent on the diameters due to polydispersity and the shape mismatch, including the charge wouldn't improve the description of the depletion interaction. Looking at Fig. 3 we see that the measured distributions are not drastically different, strengthening the conclusion, that charge is negligible here.

4 Conclusion

TIRF, in combination with particle tracking, is used to map a sphere–wall interaction potential. While not being fundamentally different from TIRM, it offers the advantages of removing background scattering almost completely and yielding high enough intensities for smaller particle sizes.

We are able to measure depletion forces by plate-like gibbsite particles for the first time. A theoretical prediction is successfully extended to encompass polydispersity of the depletant. The modified model for depletion caused by cylindrical discs fits the measured data sets nearly perfectly. The approach of an averaged potential enables us to find an estimate for the parameters of the size distribution of the depletant by means of an optical measurement. We show that the theory, in spite of non ideal platelets, is well suited to describing depletion caused by gibbsite platelets and that polydispersity has an imperceptible influence on the contact value.

Acknowledgements

The authors acknowledge financial support from the EU through FP7, project Nanodirect (Grant No. NMP4-SL-2008-213948).

References

1 F. Oosawa and S. Asakura, *The Journal of Chemical Physics*, 1954, **22**, 1255–1255.
2 D. Kleshchanok, R. Tuinier and P. R. Lang, *J. Phys.: Condens. Matter*, 2008, **20**, 073101.
3 A. Kulkarni and C. Zukoski, *J. Cryst. Growth*, 2001, **232**, 156–164.
4 C. Gögelein, PhD thesis, Heinrich-Heine-Universität-Düsseldorf, 2008.
5 B. Neu and H. Meiselman, *Biophys. J.*, 2002, **83**, 2482–2490.
6 R. Roth and R. Evans, *Europhys. Lett.*, 2001, **53**, 271.
7 Y.-L. Chen and K. S. Schweizer, *J. Chem. Phys.*, 2002, **117**, 3.
8 S. Asakura and F. Oosawa, *J. Polym. Sci.*, 1958, **33**, 183–192.
9 Y. Mao, M. Cates and H. Lekkerkerker, *J. Chem. Phys.*, 1997, **106**, 3721–3729.
10 D. Kleshchanok, R. Tuinier and P. R. Lang, *Langmuir*, 2006, **22**, 9121–9128.
11 Y. K. Leong, *Colloids Surf., A*, 1996, **118**, 107–114.
12 P. Holmqvist, D. Kleshchanok and P. R. Lang, *Eur. Phys. J. E*, 2008, **26**, 177–182.
13 P. Holmqvist, D. Kleshchanok and P. R. Lang, *Langmuir*, 2007, **23**, 12010–12015.
14 K.-H. Lin, J. C. Crocker, A. C. Zeri and A. G. Yodh, *Phys. Rev. Lett.*, 2001, **87**, 088301.
15 L. Helden, G. H. Koenderink, P. Leiderer and C. Bechinger, *Langmuir*, 2004, **20**, 5662–5665.
16 L. Helden, R. Roth, G. H. Koenderink, P. Leiderer and C. Bechinger, *Phys. Rev. Lett.*, 2003, **90**, 048301.
17 H. V. Olphen, *An introduction to clay colloid chemistry*, Wiley, NY, 1977.
18 H. Z. Cummins, *J. Non-Cryst. Solids*, 2007, **353**, 3891–3905.
19 H. H. Murray, *Appl. Clay Sci.*, 2000, **17**, 207–221.
20 G. Maitland, *Curr. Opin. Colloid Interface Sci.*, 2000, **5**, 301–311.
21 A. M. Wierenga, T. A. J. Lenstra and A. P. Philipse, *Colloids Surf., A*, 1998, **134**, 359–371.
22 Z. Dogic and S. Fraden, *Curr. Opin. Colloid Interface Sci.*, 2006, **11**, 47–55.
23 C. July and P. R. Lang, *Langmuir*, 2010, **26**, 18647–18651.
24 F. M. van der Kooij, K. Kassapidou and H. N. W. Lekkerkerker, *Nature*, 2000, **406**, 868–871.
25 L. Helden, PhD thesis, Universität Konstanz, 2003.
26 W. N. Everett, R. E. Beckham, K. Meissner and M. A. Bevan, *Langmuir*, 2007, **23**, 8950–8956.
27 D. C. Prieve and N. A. Frej, *Langmuir*, 1990, **6**, 396–403.
28 D. Prieve, *Adv. Colloid Interface Sci.*, 1999, **82**, 93–125.
29 D. Rudhardt, C. Bechinger and P. Leiderer, *Phys. Rev. Lett.*, 1998, **81**, 1330–1333.
30 X. Xing, Z. Li and T. Ngai, *Macromolecules*, 2009, **42**, 7271–7273.
31 G. E. Fernandes, D. J. Beltran-Villegas and M. A. Bevan, *Langmuir*, 2008, **24**, 10776–10785.
32 P. C. Odiachi Jr. and D. C. Prieve, *Colloids Surf., A*, 1999, **146**, 315–328.
33 B. Ruzicka, E. Zaccarelli, L. Zulian, R. Angelini, M. Sztucki, A. Moussaïd, T. Narayanan and F. Sciortino, *Nat. Mater.*, 2011, **10**, 56–60.
34 B. Ruzicka, L. Zulian, E. Zaccarelli, R. Angelini, M. Sztucki, A. Moussaïd and G. Ruocco, *Phys. Rev. Lett.*, 2010, **104**, 085701.
35 M. Piech and J. Y. Walz, *J. Colloid Interface Sci.*, 2000, **232**, 86–101.
36 L. Helden, E. Eremina, N. Riefler, C. Hertlein, C. Bechinger, Y. Eremin and T. Wriedt, *Appl. Opt.*, 2006, **45**, 7299–7308.
37 N. Riefler, E. Eremina, C. Hertlein, L. Helden, Y. Eremin, T. Wriedt and C. Bechinger, *J. Quant. Spectrosc. Radiat. Transfer*, 2007, **106**, 464–474.
38 J. C. Crocker and D. G. Grier, *J. Colloid Interface Sci.*, 1996, **179**, 298–310.
39 S. M. Oversteegen and H. N. W. Lekkerkerker, *Phys. Rev. E: Stat. Phys., Plasmas, Fluids, Relat. Interdiscip. Top.*, 2003, **68**, 021404.
40 P. R. Lang, *J. Chem. Phys.*, 2007, **127**, 124906.
41 J. E. G. J. Wijnhoven, *Chem. Mater.*, 2004, **16**, 3821–3828.
42 D. D. Lide, *CRC Handbook of Chemistry and Physics, 91*, Taylor and Francis Group, LLC, 2010.
43 M. Piech and J. Y. Walz, *Langmuir*, 2000, **16**, 7895–7899.

